Measurement of thermal diffusivity of air using photopyroelectric interferometry

Chinhua Wang and Andreas Mandelis[a)]
Photothermal and Optoelectronic Diagnostics Laboratories (PODL), Department of Mechanical and Industrial Engineering, University of Toronto, Toronto, Ontario M5S 3G8, Canada

(Received 9 November 1998; accepted for publication 9 February 1999)

A new photopyroelectric (PPE) method for measuring the thermal diffusivity of ambient gases with optimal precision is introduced. The technique is based on destructive PPE interferometric detection inside a thermal-wave resonant cavity with an optically transparent wall. A new PPE sensor design generating purely thermal-wave interference is used to improve the signal-to-noise ratio and the measurement dynamic range and precision by suppressing the large optically transmitted base line signal. Cavity-length scanning is employed and the thermal diffusivity of air is measured with third-significant-figure precision. Comparisons of measurement precision are made with experimental results obtained using a transparent-wall PPE thermal-wave cavity in the single-ended (noninterferometric) mode. The physical signal generation mechanisms are also discussed. © *1999 American Institute of Physics.* [S0034-6748(99)04505-0]

I. INTRODUCTION

Photothermal and photoacoustic techniques have been used successfully in studies of optical and thermophysical properties of solids as nondestructive evaluation methodologies.[1–5] Recent developments in monitoring and measuring the properties of gases using photothermal techniques have attracted much attention for environmental quality control and manufacturing safety reasons.[6–9] Specifically, a newly developed[8] thermal-wave resonant cavity (TWRC) sensor using a pyroelectric thin-film transducer (polyvinylidene fluoride, PVDF) proved to offer a powerful method for measuring the thermal diffusivities of gases with very high precision and gas-species resolution.[9–12] A thermal-wave cavity consists of two parallel walls: one wall is usually an opaque thin metallic foil, which is periodically heated using either a laser beam or direct ac electrical (resistive) heating; the other wall consists of the PVDF transducer itself at a distance L from the thermal-wave source wall. By scanning the cavity-length L, one can obtain resonance-like extrema in both lock-in in-phase (IP) and quadrature channels of the output (photo)pyroelectric signal. Based on mechanisms of conduction and radiation heat transfer across the intracavity space,[10] these signal extrema can be used for a simultaneous measurement of the thermal diffusivity and thermal conductivity of the intracavity gas or vapor. The values of thermal diffusivity thus obtained are of the highest precision to date.[12] In part this is due to the high signal-to-noise ratio (SNR) effected by the cavity-length scanning process: the single modulation frequency used throughout the cavity scan results in constant output noise bandwidth, whereas the constant-cavity-length frequency scans result in variable noise bandwidth with compromised SNR.[9] It is, however, possible to further reduce the TWRC device noise and substantially enhance the signal generation dynamic range by means of a novel thermal-wave-interferometric design.[13] The implementation of this sensor design has allowed the use of a transparent wall in the TWRC. Unlike the earlier (''conventional'') opaque walls used with this device[8–12] for gas-phase thermophysical measurements, a transparent wall can efficiently extend the utility of the TWRC to include the measurement of *both* optical and thermophysical properties of materials. With a single cavity this can only be done at the expense of sensitivity to the thermal component of the signal, owing to the strong direct laser-beam transmission to, and photothermal conversion at, the PVDF element which usually dominates the overall PPE signal.[1] Earlier attempts to eliminate this direct signal component from PPE spectroscopic investigations include lock-in quadrature detection. This technique has been successful in suppressing the direct transmitted PPE signal by up to two orders of magnitude,[14,15] but problems remain with uncompensated detector noise and signal drift from the lock-in IP to quadrature (Q) channel, especially related to the dc heating of the PVDF transducer.

In this article, we introduce a novel PPE sensor principle for spectroscopic applications based on destructive thermal-wave interference. The general theoretical framework of photopyroelectric interferometry was presented in Ref. 13, including the physical mechanism of signal generation. In the present work, we focus on the design and operation of the PPE setup, especially the signal-to-noise advantage of the dual-beam versus the single-beam configuration. The interferometric sensor represents an alternative method for measuring the thermal diffusivity of the intracavity gas. Instead of an opaque wall, a transparent material wall is employed. The replacement of the opaque wall[8–12] with a transparent one is dictated by the intended use of the new PPE instrument as a spectroscopic detector operating under a photo-

a)Electronic mail: mandelis@mie.utoronto.ca

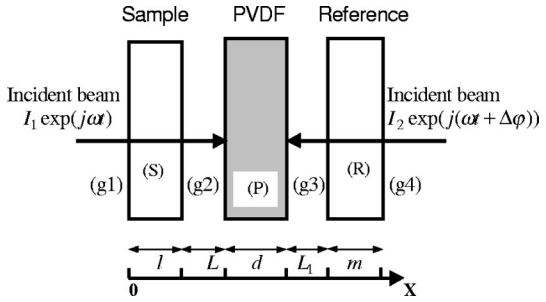

FIG. 1. Geometry of a dual-cavity PPE interferometer.

thermal PPE signal generation mechanism within the thermal-wave cavity. The recently introduced purely thermal-wave interferometric technique[13] is used to improve the signal-to-noise ratio and the measurement dynamic range by suppressing the substantial transmission base line.

II. PPE INTERFEROMETRIC SENSOR DESIGN AND SIGNAL THEORY

Figure 1 shows the most general outline of the purely thermal-wave interferometric PPE sensor. Two laser beams (intensities are I_1 and I_2), are split off of a single laser beam with a beamsplitter. They are modulated with a mechanical chopper at the same frequency (ω) and with a fixed, adjustable phase shift ($\Delta\varphi$). The beams are incident onto the front and rear surfaces of a PVDF detector passing through a fully or partly transparent wall (or solid sample) and a transparent reference medium, respectively. The thicknesses of the sample/front wall, the reference and the PVDF are *l*, *m*, and *d*, respectively, and the cavity lengths formed by the sample PVDF and the PVDF reference are L and L_1, respectively. The overall output PPE signal from the PVDF detector is the interferometric result of several contributions: (1) the direct optical transmission of incident light passing through the sample/front wall and through the reference/back wall, (2) thermal-wave confinement effects resulting from the direct transmission of incident light onto the PVDF detector and the presence of the two thermal-wave cavities, (3) conduction heat transfer from the sample and the reference to the PVDF due to optical absorption and subsequent optical-to-thermal energy conversion processes in the sample and the reference. Radiation heat transfer has been observed at large cavity lengths with single TWRC PVDF sensors,[10,16] but it can be safely neglected for the short cavity lengths utilized with the present interferometric PPE system. A theoretical model of the photopyroelectric signal generation in the geometry of Fig. 1 has been developed.[13] The resulting signal corresponding to the most general dual-cavity interferometric geometry of Fig. 1 is given by the following expression:

$$V(\omega)=\frac{S(\omega)}{\sigma_p(1+b_{2p})(1+b_{3p})} \times\frac{H_1(1+b_{3p})[G_1(1+W_{21}e^{-2\sigma_2 L})+2b_{2p}G_3e^{-\sigma_2 L}]+H_2(1+b_{2p})[G_2(1+V_{34}e^{-2\sigma_3 L_1})+2b_{3p}G_4e^{-\sigma_3 L_1}]}{[e^{\sigma_p d}(1+\gamma_{3p}V_{34}e^{-2\sigma_3 L_1})(1+\gamma_{2p}W_{21}e^{-2\sigma_2 L})-e^{-\sigma_p d}(\gamma_{2p}+W_{21}e^{-2\sigma_2 L})(\gamma_{3p}+V_{34}e^{-2\sigma_3 L_1})]}, \quad (1)$$

where

$$\sigma_i=(1+j)\sqrt{\omega/2\alpha_i}, \quad j^2=-1, \quad (1a)$$

$$b_{ij}=k_i\sqrt{\alpha_j}/k_j\sqrt{\alpha_i}, \quad (1b)$$

$$\gamma_{ij}=(1-b_{ij})/(1+b_{ij}), \quad (1c)$$

$$W_{21}=-\frac{\gamma_{2s}e^{\sigma_s l}-\gamma_{1s}e^{-\sigma_s l}}{e^{\sigma_s l}-\gamma_{2s}\gamma_{1s}e^{-\sigma_s l}}, \quad (1d)$$

$$V_{34}=-\frac{\gamma_{3r}e^{\sigma_r m}-\gamma_{4r}e^{-\sigma_r m}}{e^{\sigma_r m}-\gamma_{3r}\gamma_{4r}e^{-\sigma_r m}}, \quad (1e)$$

$$G_1=\frac{(1-R_p)}{k_p\sigma_p}\times\frac{I_1(1-R_s)^2}{1-R_s^2e^{-2\beta_s l}}e^{-\beta_s l}, \quad (1f)$$

$$G_2=\frac{(1-R_p)}{k_p\sigma_p}\times\frac{I_2e^{j\Delta\varphi}(1-R_r)^2}{1-R_r^2e^{-2\beta_r m}}e^{-\beta_r m}. \quad (1g)$$

In Eqs. (1)–(1g), subscripts $i,j=1,2,3,4,s,p,r$ represent regions $g1$, $g2$, $g3$, $g4$, *S*, *P* and *R*, respectively. R_i represents the surface optical reflectivity of medium $i(i=s,p,r)$; α_i, k_i are the thermal diffusivity and heat conductivity of medium i; β_s,β_r are optical absorption coefficient of the sample and the reference, respectively. H_1, H_2 are given as follows:

$$H_1=(e^{\sigma_p d}-1)(1+\gamma_{3p}V_{34}e^{-2\sigma_3 L_1}) +(1-e^{-\sigma_p d})(\gamma_{3p}+V_{34}e^{-2\sigma_3 L_1}), \quad (1h)$$

$$H_2=(e^{\sigma_p d}-1)(1+\gamma_{2p}W_{21}e^{-2\sigma_2 L}) +(1-e^{-\sigma_p d})(\gamma_{2p}+W_{21}e^{-2\sigma_2 L}). \quad (1i)$$

G_3, G_4 represent the optical absorption and subsequent optical-to-thermal conversion contribution of the sample and the reference to the overall PPE signal, respectively. They are given in detail in the Appendix, where η_s,η_r are the optical-to-thermal conversion coefficients of the sample and the reference, respectively [Eqs. (A5) and (A13)].

Various measurement configurations can be obtained by using different combinations of the (optically transparent or opaque) sample and the reference, as well as the front and the rear laser beams. For the purposes of the present experiments, the entire system is assumed to be exposed to a uniform gaseous ambient in order to measure the thermal diffusivity of the gas, i.e., $g1=g2=g3=g4=g$ in Fig. 1 and in Eq. (1). Owing to the significant complexity of the structure

of Eq. (1), it is instructive to consider several special (limiting) cases of experimental relevance with regard to the geometric configuration of the system and the opacity of the cavity wall(s). The resulting equations are much simpler and more amenable to physical qualitative and quantitative analysis.

A. Single-beam measurement scheme

In this special geometry the PVDF element is considered to be semi-infinite, i.e., $e^{-\sigma_p d}\to 0$, since the PPE system is not interferometric in the absence of the rear beam, and the laser chopping frequencies used ($f>20$ Hz) are such that the PVDF sensor is thermally thick.[17] Therefore, without loss of generality, the single-ended (conventional) PPE signal output can be simplified in Eq. (1) and expressed as

$$V(\omega)=C(\omega)\times\frac{G_1(1+W_{21}e^{-2\sigma_g L})+2b_{\rm gp}G_3e^{-\sigma_g L}}{1+\gamma_{\rm gp}W_{21}e^{2\sigma_g L}}, \tag{2}$$

where

$$W_{21}=-\gamma_{\rm gs}\frac{1-e^{-2\sigma_s l}}{1-\gamma_{\rm gs}^2e^{-\sigma_s l}}. \tag{3}$$

The terms $\sigma_g, b_{\rm gp}, \gamma_{\rm gp}$, G_1 and G_3 are defined in Eqs. (1). G_1 represents the contributions of direct optical transmission of incident light onto the PVDF surface of reflectivity R_p. G_3 represents heat conduction from the sample/wall to the PVDF due to optical absorption in the sample/wall. $C(\omega)$ is a complex-valued instrumental quantity, which involves the frequency response (transfer function) of the PPE system. For cavity-length scans $C(\omega)$ is a normalization constant. Depending on whether the cavity wall is optically opaque or transparent, the following two special subcases are obtained:

1. Case A.1. Optically opaque cavity wall

If the cavity wall is optically opaque, there is no direct optical transmission of the incident laser light onto the PVDF element. Therefore, the output PPE signal is obtained by setting $G_1=0$ in Eq. (2)

$$V(\omega)=C_1(\omega)\times\frac{e^{-\sigma_g L}}{1+\gamma_{\rm gp}W_{21}e^{-2\sigma_g L}}, \tag{4}$$

where $C_1(\omega)$ is a complex-valued constant independent of cavity-length L. This result is the same as that used in describing the mechanism of the conventional TWRC sensor.[8–10]

2. Case A.2. Optically transparent cavity wall

In this case, direct optical transmission through the sample, and heat generation following optical absorption in the sample, both contribute to the overall output PPE signal. However, theoretical simulations of Eq. (2) show that the contribution of heat conduction from the sample to the PVDF generates a thermal-wave signal about three-to-four orders of magnitude smaller than that due to direct optical transmission. Therefore, the overall output PPE signal is obtained by neglecting the second term in Eq. (2)

$$V(\omega)=C_2(\omega)\times\frac{I_1(1+W_{21}e^{-2\sigma_g L})}{1+\gamma_{\rm gp}W_{21}e^{-2\sigma_g L}} \tag{5a}$$

or

$$V(\omega)=C_2(\omega)\times I_1\left[1+\frac{W_{21}(1-\gamma_{\rm gp})e^{-2\sigma_g L}}{1+\gamma_{\rm gp}W_{21}e^{-2\sigma_g L}}\right], \tag{5b}$$

where I_1 is the intensity of the incident laser beam, and $C_2(\omega)$ is a complex-valued constant.

B. Two-beam measurement scheme (pure thermal-wave destructive interferometry)

In the foregoing case of single-ended detection with an entirely transparent cavity wall on the sample side, Eq. (5) shows that the PPE signal consists of two components: the first term is a cavity-length independent factor. The second term depends on cavity length, but is much smaller than the first term by about two orders of magnitude. Therefore, a very large base line signal stemming from the first term always accompanies measurements, and thus limits measurement sensitivity, reproducibility and dynamic range in the single-beam configuration. The newly developed pure thermal-wave photopyroelectric interferometric technique[13] provides a suitable method for suppressing this large base line signal. The result is a substantial improvement in SNR, reproducibility and signal dynamic range.

1. Case B. Optically transparent wall using pure thermal-wave destructive interferometry

For simplicity, we only consider the relatively simple case, in which an out-of-phase laser beam is incident onto the rear surface of the PVDF without the presence of a reference sample. Therefore, the cavity-length dependent PPE signal is found from Eq. (1) to be

$$V(\omega)=C_3(\omega)\,\frac{Q_1(1+W_{21}e^{-2\sigma_g L})+Q_2(1+\gamma_{\rm gp}W_{21}e^{-2\sigma_g L})}{(1+\gamma_{\rm gp}W_{21}e^{-2\sigma_g L})}, \tag{6}$$

where

$$Q_1=\frac{I_1(1-R_s)^2}{1-R_s^2e^{-2\beta_s l}}e^{-\beta_s l},\quad Q_2=I_2e^{j\Delta\varphi}. \tag{7}$$

R_s is the surface reflectance of the sample, β_s is the optical absorption coefficient of the sample at the excitation wavelength, l is the thickness of the sample, and $\Delta\varphi$ is the phase shift between the two beams. In Eq. (6), the contribution of heat conduction from the sample to the PVDF has been neglected due to its small size when compared with other thermal sources. Equation (6) shows that the large base line signal Q_1 can be completely suppressed by another cavity-length independent term Q_2 upon adjustment of the relative intensities *and* the phase shift between the two beams such that $Q_1=-Q_2$ when the sample is placed far away from the PVDF (i.e., in the thermally thick range). In practice, this can be achieved by adjusting I_1, I_2 and $\Delta\varphi$ such that the demodulated PPE signal in the lock-in amplifier is zero when

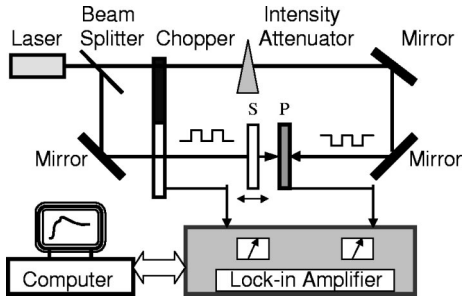

FIG. 2. Schematic diagram of PPE interferometric experimental setup. S: sample; P: pyroelectric element.

the sample is >5 mm away from the PVDF and $\Delta\phi=\pi$. After suppression of the large base line signal, the PPE output signal becomes

$$V(\omega)=C_4(\omega)\times\frac{I_1W_{21}(1-\gamma_{\rm gp})e^{-2\sigma_gL}}{1+\gamma_{\rm gp}W_{21}e^{-2\sigma_gL}}. \tag{8}$$

Comparing Eq. (8) with Eq. (5b), operationally we can obtain the former by simply dropping the unity inside the brackets in Eq. (5b). This is, however, significant from the experimental point of view. As mentioned above, the cavity-length dependent term in Eq. (5) is approximately two orders of magnitude less than the unity. As a result, the measurement sensitivity to the parameters of the ratio inside the brackets, to signal dynamic range and to SNR is compromised. In contrast, a much higher instrumental sensitivity can be achieved in the thermal-wave interferometric mode due to the coherent suppression of the large base line signal within the PVDF detector. Moreover, the signal noise due to fluctuations of the laser power can also be cancelled out in real time in destructive thermal-wave interferometry, since $Q_2=-Q_1$.

III. EXPERIMENT AND RESULTS

The schematic diagram of a general PPE experimental setup is shown in Fig. 2. A transparent Ti-sapphire disk sample, 0.1295 cm thick was used as a cavity wall. The sample was mounted on the micrometer stage (10 μm resolution), allowing scanning of the cavity length formed by the sample and the PVDF surface. The relative intensities of the front and back incident beams were adjusted by a linear intensity attenuator and the phase shift between the two beams was precisely controlled by a mechanical chopper (EG&G Model 192), also fixed on a micrometer stage. A disk-shaped PVDF film, 52 μm thick and 1.2 cm in diameter, was installed on an aluminum-base bearing a hole. The PVDF element acted as thermal-wave signal transducer and as a wall for front and back thermal-wave cavities. The PPE signal from the PVDF was fed into a lock-in amplifier (EG&G model 5210), which was controlled by a PC. Single-beam or two-beam measurements could be performed by either blocking or unblocking the rear laser beam, respectively. Experiments were conducted as follows: for single-beam measurements the rear beam was blocked. This is similar to the experimental mode reported earlier,[8,9] except for the transparent wall in the present circumstance. The purely thermal-wave interferometric technique was introduced to suppress the large base line signal by employing the rear beam, which was adjusted to 180° phase shift with respect to the front laser beam. The sample was first placed at a far distance from the PVDF compared to the thermal diffusion length in the cavity. The relative intensities between the two beams were then adjusted, such that the output PPE lock-in signal was zero. Finally, the sample-PVDF distance was scanned and the output signal was recorded versus the cavity-length L.

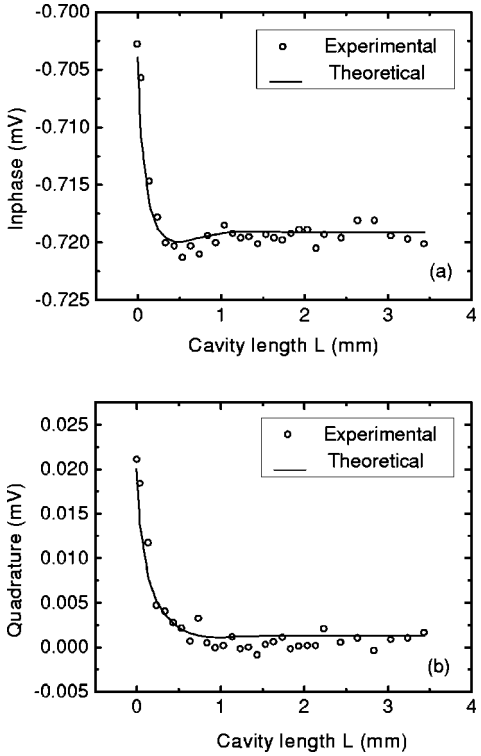

FIG. 3. PPE experimental data and theoretical fits vs thermal-wave cavity length L at a modulation frequency $f=26.6$ Hz, using single-beam detection with a transparent Ti-sapphire cavity wall. The best-fit value of the thermal diffusivity of air was $\alpha_g=0.21\pm0.02$ cm^2/s at $T=295$ K. (a) In-phase and (b) quadrature lock-in channel data.

Figure 3 shows typical experimental results using the single-beam method, in a configuration corresponding to Case A.2 The modulation frequency, *f*, was 26.6 Hz. By fitting the experimental data of the lock-in quadrature channel to Eq. (5), the thermal diffusivity of room temperature air was found to be 0.21 ± 0.02 cm^2 s^{-1}, the average of four measurements. The other parameters used in Eq. (5) are $k_g=2.62\times10^{-4}$ W cm$^{-1}\cdot$K^{-1}, $k_s=0.33$ W cm$^{-1}\cdot$K^{-1}, $k_p=1.3\times10^{-3}$ W cm$^{-1}\cdot$K^{-1}, $\alpha_s=0.106$ cm^2 s^{-1} and $\alpha_p=5.4\times10^{-4}$ cm^2 s^{-1},[1] respectively. Figure 4 shows experimental results using the destructive interferometric configuration, Case B. The experimental conditions were the same as those used with the single-beam method, but the data quality and the SNR are clearly superior to the single-ended case. Fitting the experimental data to Eq. (8) yielded the value $\alpha_g=0.219\pm0.003$ cm^2 s^{-1}, the average of four measurements, for the room-temperature thermal diffusivity of air.

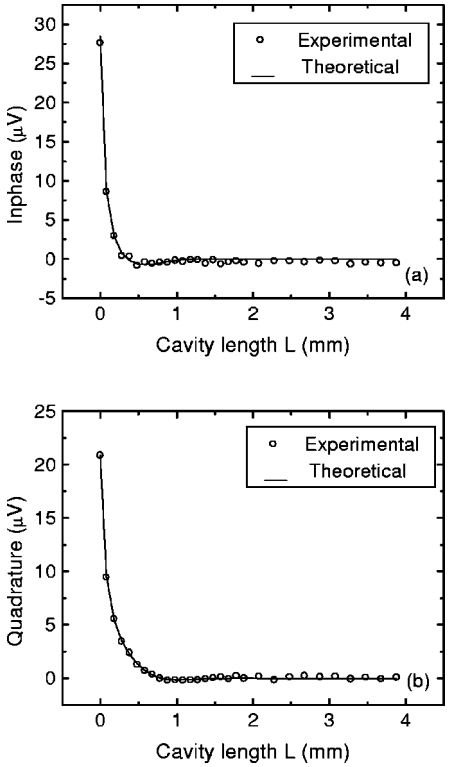

FIG. 4. PPE experimental and theoretical fits vs thermal-wave length L at a modulation frequency $f=26.6$ Hz, using pure thermal-wave destructive interferometry. The best-fit value of the thermal diffusivity of air was $\alpha_g = 0.219 \pm 0.003$ cm^2/s at $T=295$ K. (a) In-phase and (b) quadrature lock-in channel data.

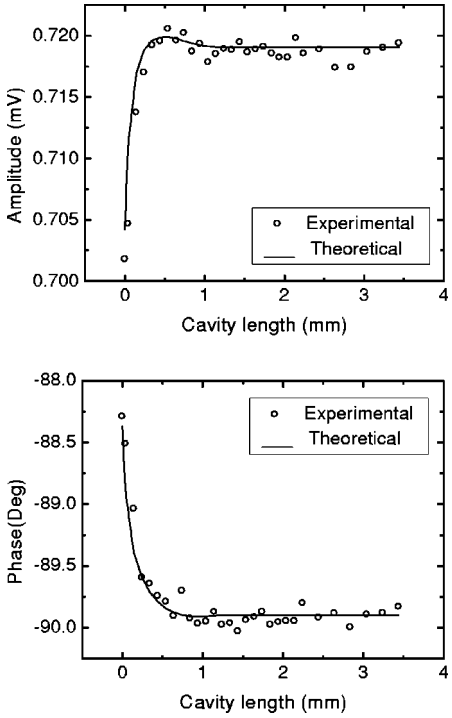

FIG. 5. Spatial profiles of the amplitude (a) and phase (b) of the PPE signal using a single-beam configuration, with a Ti-sapphire transparent cavity wall (thickness l=0.1295 cm; frequency f=26.6 Hz).

IV. DISCUSSION

The transparent-wall thermal-wave cavity measurements of room-temperature air thermal diffusivity agree very well with those using a TWRC with an opaque exterior wall.[8–10] Furthermore, both results are in good agreement with literature values lying in the range of 0.19–0.228 cm^2 s^{-1}.[13–15] The standard deviation of α_g is about 10% for the single-beam method, but it is only approximately 1.3% for the dual-beam destructive interferometric measurement. The SNR and the measurement precision of thermal-wave interferometry using transparent exterior walls is comparable with results using a single-ended TWRC cavity with opaque external wall ($\sim 1\%$). This can be explained as follows: in the case of the TWRC with an opaque wall, the thermal waves launched by the wall material following optical-to-thermal energy conversion are completely cavity-length dependent with no base line signal. Therefore, a very high instrumental sensitivity can be attained. Furthermore, the noise due to any fluctuations in the incident laser power is reduced to a large extent, by time averaging through the (low-pass-filter-equivalent) slow thermal transfer process. In the case of the single-ended TWRC with a transparent exterior wall, the large base line signal due to direct optical transmission substantially limits instrumental sensitivity and signal dynamic range. This signal is not immune to fluctuations in the incident laser power, which further deteriorate the SNR and hence the measurement fidelity. The real-time cancellation of the direct-transmission-generated base line signal and of much of the random optical fluctuation in PPE destructive interferometry resembles the absence of optical base line and the time averaging of fast random fluctuations in the single-ended opaque-wall TWRC configuration. Therefore, it is expected, at least qualitatively, that the SNRs of the two configurations should be comparable. It is also expected that both SNRs should be much better than the single-beam TWRC configuration with a transparent exterior wall. This expectation is borne out by direct comparison of the data quality in Figs. 3 and 4. In the case of an optically opaque wall, the sole thermal source within the cavity is the optical-to-thermal energy conversion process occurring in that wall/sample. Therefore, the thermal-wave power received by the PVDF detector is a monotonically increasing function of the decreasing cavity length as a result of the energy confinement in the cavity.[10] In the case of a transparent cavity wall, however, the thermal source due to optical absorption by the sample/wall contributes only a very small portion to the overall PPE signal, when compared with the direct transmission of the incident light onto the PVDF detector. Since the overall PPE signal substantially comes from the direct optical absorption of the transmitted light onto the PVDF detector itself, it should be largely independent of the distance between sample and PVDF surface, i.e., cavity length L. However, both theoretical and experimental data, Fig. 5, show that the PPE signal actually becomes a function of L at short cavity lengths within a thermal diffusion length. The same Ti-sapphire disk as that in Figs. 3 and 4 was used in Fig. 5. It is seen that the amplitude of the PPE signal is indeed independent of the cavity length when the cavity is longer than 2 mm. Then it rises, reaching a maximum, followed by a rapid drop when the cavity length is less than

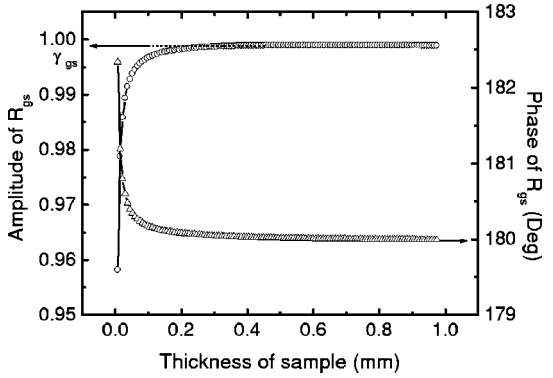

FIG. 6. Complex thermal wave reflection coefficient at gas-solid boundary vs thickness of the solid. Parameters used are: $k_g=2.62\times10^{-4}$ W/cm K, $\alpha_g=0.22$ cm^2/s, $k_s=0.33$ W/cm K, $\alpha_s=0.106$ cm^2/s, and $f=10$ Hz.

$\sim$0.5 mm. This phenomenon is associated with the coherent superposition of two thermal waves, both generated at the surface of the PVDF layer through direct optical absorption, and through ''reflection''[18,19] at the nearby surface of the sample, when the latter is well within one thermal diffusion length away. The phases of the two waves at the surface of the PVDF sensor are such that they result in decreasing of the thermal-wave field there. This is further borne out by examination of the first and second terms inside the bracket of the relevant theoretical formula, Eq. (5). The structure of that expression shows that the first term can be explained as the direct PVDF-surface contribution and the second term as the contribution from the reflected portion, which after a round trip and a reflection at the gas-sample boundary, interferes with the direct PVDF surface thermal wave. The term *reflection* is only used for convenience. It implies that the thermal-wave field within the cavity can *mathematically* be considered as the superposition of forward and reflected waves, whereas physically any concept of reflection conflicts with the unidirectionality of the Fourier equation of diffusion.[8,13] Nevertheless, consistently with its mathematical definition,[18,19] the thermal wave reflection coefficient $R_{\rm gs}$ at the gas-sample boundary in Eq. (5) is

$$R_{\rm gs}=W_{21}=-\gamma_{\rm gs}\frac{1-e^{-2\sigma_s l}}{1-\gamma_{\rm gs}^2 e^{-\sigma_s l}}. \tag{9}$$

Equation (9) shows that the thermal wave reflection coefficient $R_{\rm gs}$ is not only a function of the thermal properties of the two media which form the boundary interface, but also of the thickness of the medium from which the thermal wave is reflected (or, more accurately, in which it is confined). This is, essentially, a thermal-wave impedance. Obviously, if the thickness of the sample is zero, i.e., absence of the sample

$$R_{\rm gs}=0. \tag{10}$$

If the sample is semi-infinite, then the reflection coefficient reduces to

$$R_{\rm gs}=-\gamma_{\rm gs}, \tag{11}$$

which is the same as the definition given earlier.[18,19] The negative sign ''$-$'' in Eq. (11) implies that there is a 180° phase shift for thermal waves reflecting from the gas-sample boundary. Figure 6 shows the thermal wave reflection coefficient $R_{\rm gs}$ versus the thickness of the sample. The thermophysical parameters of air and Ti-sapphire material were used for this simulation. It can be seen that the semi-infinite sample reflection coefficient defined in Refs. 18,19, and in Eq. (11) is valid for most of the gas-solid boundary in which the solid material is thicker than a few hundred microns. The sample thickness does matter if the solid is thinner than the thermal diffusion length in the material (a few tens microns).

Based on the convenient concept of thermal-wave reflection coefficient, the overall PPE signal in Fig. 5 is actually a superposition of thermal waves that are originally produced within the PVDF and those reflected from the sample. A constant output in the amplitude channel when the sample is at a far distance away from the PVDF is due to the fact that the reflected portion is substantially zero owing to the highly damped nature of the thermal waves. As the interface approaches within one thermal diffusion length, the thermal waves exhibit a shallow constructive superposition at the location where the phase is restored to its original value after one round trip. As the cavity length further decreases, the contribution from the reflected thermal-wave power increases, while the overall phase moves away from the constructive interference condition, therefore resulting in an overall decrease of the amplitude on the PVDF surface.

ACKNOWLEDGMENT

The authors gratefully acknowledge a Research Grant from the Natural Sciences and Engineering Research Council of Canada.

APPENDIX: DEFINITIONS OF EXPRESSIONS

$$G_3=\frac{2B_1-B_2(1+b_{1s})e^{\sigma_s l}+B_3(1-b_{1s})e^{-\sigma_s l}}{(1+b_{1s})(1+b_{2s})(e^{\sigma_s l}-\gamma_{1s}\gamma_{2s}e^{-\sigma_s l})}, \tag{A1}$$

with

$$B_1=E_s[b_{1s}(N_1+N_2e^{-2\beta_s l})+r_s(N_1-N_2e^{-2\beta_s l})], \tag{A2}$$

$$B_2=E_s e^{-\beta_s l}[N_1+N_2+r_s(N_1-N_2)], \tag{A3}$$

$$B_3=E_s e^{-\beta_s l}[N_1+N_2-r_s(N_1-N_2)], \tag{A4}$$

$$E_s=\frac{I_1\eta_s\beta_s}{2k_s(\beta_s^2-\sigma_s^2)}\cdot\frac{1-R_s}{1-R_s^2e^{-2\beta_s l}}, \tag{A5}$$

$$r_s=\beta_s/\sigma_s, \tag{A6}$$

$$N_1\equiv 1+R_sR_p(1+R_s)e^{-2\beta_s l}, \tag{A7}$$

$$N_2\equiv R_s[1+R_p(1+R_s)] \tag{A8}$$

and

$$G_4=\frac{2P_1+P_2(1+b_{4r})e^{\sigma_r m}-P_3(1-b_{4r})e^{-\sigma_r m}}{(1+b_{3r})(1+b_{4r})(e^{\sigma_r m}-\gamma_{3r}\gamma_{4r}e^{-\sigma_r m})}, \tag{A9}$$

with

$$P_1=E_r[b_{4r}(N_{1r}+N_{2r}e^{-2\beta_r m})+r_r(N_{1r}-N_{2r}e^{-2\beta_r m})], \tag{A10}$$

$$P_2=-E_r e^{-\beta_r m}[N_{1r}+N_{2r}+r_r(N_{1r}-N_{2r})], \tag{A11}$$

$$P_3=-E_r e^{-\beta_r m}[N_{1r}+N_{2r}-r_r(N_{1r}-N_{2r})], \tag{A12}$$

$$E_r = \frac{I_2 e^{j\Delta\varphi}\eta_r\beta_r}{2k_r(\beta_r^2-\sigma_r^2)} \cdot \frac{1-R_r}{1-R_r^2 e^{-2\beta_r m}}, \tag{A13}$$

$$r_r = \beta_r/\sigma_r, \tag{A14}$$

$$N_{1r} \equiv 1 + R_r R_p (1+R_r) e^{-2\beta_r m}, \tag{A15}$$

$$N_{2r} \equiv R_r[1 + R_p(1+R_r)]. \tag{A16}$$

[1] A. Mandelis, J. Vanniasinkam, and S. Budhudu, Phys. Rev. B **48**, 6808 (1993).
[2] A. K. Ghosh and B. K. Chaudhuri, J. Appl. Phys. **80**, 5292 (1996).
[3] J. Philip, Rev. Sci. Instrum. **67**, 3621 (1996).
[4] J. Shen, K. Fjeldsted, J. Vanniasinkam, and A. Mandelis, Opt. Mater. **4**, 823 (1995).
[5] M. Munidasa, F. Funak, and A. Mandelis, J. Appl. Phys. **83**, 3495 (1998).
[6] A. Bozoki, J. Sneider, G. Szabo, A. Miklos, M. Serenyi, G. Nagy, and M. Feher, Appl. Phys. B: Lasers Opt. **63**, 399 (1996).
[7] M. Feher, Y. Jiang, J. P. Maier, and A. Miklos, Appl. Opt. **33**, 1655 (1994).
[8] J. Shen and A. Mandelis, Rev. Sci. Instrum. **66**, 4999 (1995).
[9] J. Shen, A. Mandelis, and B. D. Aloysius, Int. J. Thermophys. **17**, 1241 (1996).
[10] J. Shen, A. Mandelis, and H. Tsai, Rev. Sci. Instrum. **69**, 197 (1998).
[11] M. Bertolotti, G. L. Laikhou, R. li Voti, S. Paoloni, and C. Sibilia, Int. J. Thermophys. **19**, 559 (1998).
[12] J. Shen, A. Mandelis, and T. Ashe, Int. J. Thermophys. **19**, 510 (1998).
[13] C.-H. Wang and A. Mandelis, J. Appl. Phys. (in press).
[14] A. Mandelis, J. Vanniasinkam, S. Buddhudu, A. Othonos, and M. Kokta, Phys. Rev. B **48**, 6808 (1993-II).
[15] J. Shen, A. Mandelis, A. Othonos, and J. Vanniasinkam, Appl. Spectrosc. **49**, 819 (1995).
[16] G. Pan and A. Mandelis, Rev. Sci. Instrum. **69**, 2918 (1998).
[17] A. Mandelis and M. M. Zver, J. Appl. Phys. **57**, 4421 (1985).
[18] C. A. Benett, Jr. and R. R. Patty, Appl. Opt. **21**, 49 (1982).
[19] F. A. McDonald, Am. J. Phys. **48**, 41 (1980)